iScience

CellPress
OPEN ACCESS

Article

Synthesis and characterization of a Sb_2Te_3/Bi_2Te_3 p-n junction heterostructure via electrodeposition in nanoporous membranes

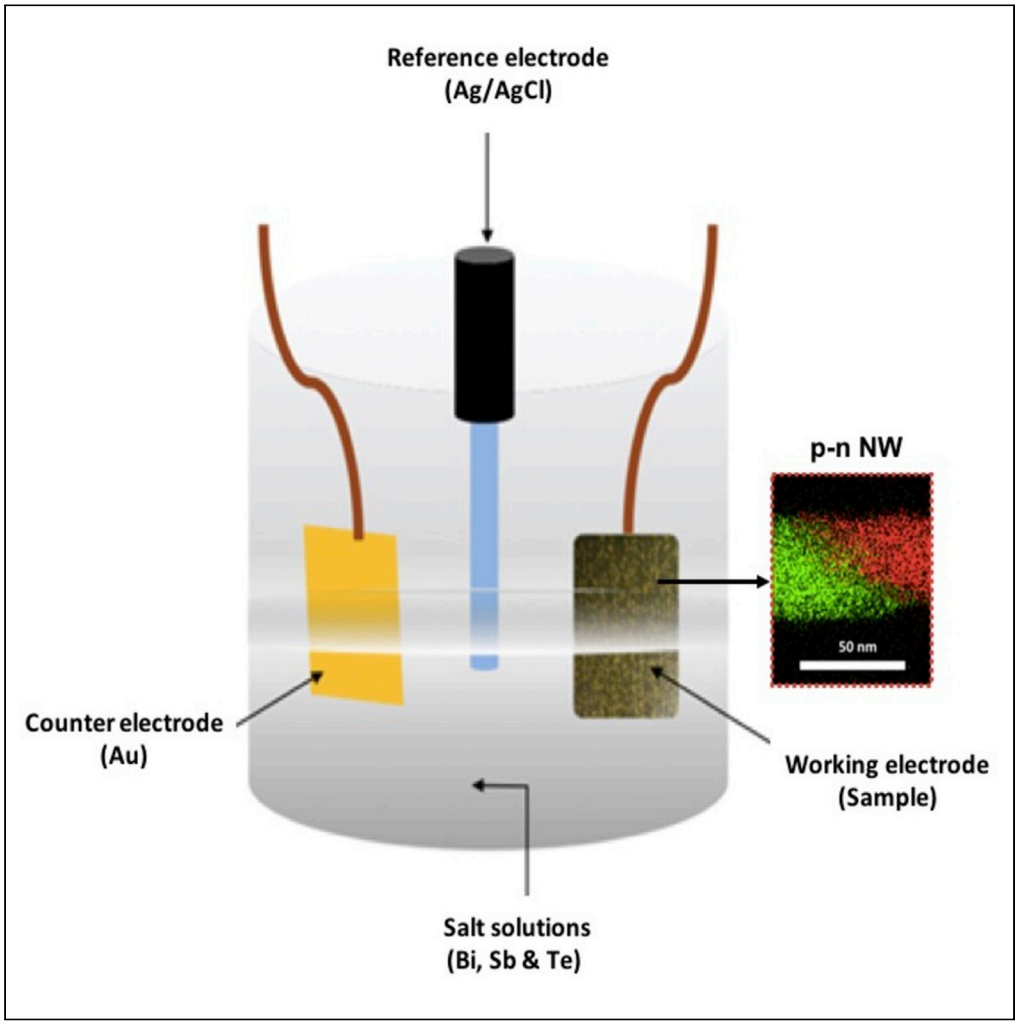

Rashmi Rani, Sandrine Tusseau-Nenez, Pierre-Eugene Coulon, Travis.L. Wade, Marcin Konczykowski

newton_rashmi51@yahoo.com

Highlights

We investigated nanostructural properties of of Bi_2Te_3, Sb_2Te_3, and p-n junction NWs

Electrodeposition is used to grow crystalline Bi_2Te_3, Sb_2Te_3, and p-n junction NWs

LHJ is identified in the transition region of the p-n junction NWs

Explicit interface is observed in the p-n junction NWs

Rani et al., iScience *24*, 102694
June 25, 2021
https://doi.org/10.1016/j.isci.2021.102694

iScience

CellPress
OPEN ACCESS

Article

Synthesis and characterization of a Sb_2Te_3/Bi_2Te_3 p-n junction heterostructure via electrodeposition in nanoporous membranes

Rashmi Rani,[1,3,*] Sandrine Tusseau-Nenez,[2] Pierre-Eugene Coulon,[1] Travis.L. Wade,[1] and Marcin Konczykowski[1]

SUMMARY

Topological insulators (TIs) are bulk insulators with metallic surface states that can be described by a single Dirac cone. However, low-dimensional solids such as nanowires (NWs) are a challenge, due to the difficulty of separating surface contributions from bulk carriers. Fabrication of NWs with high surface-to-volume ratio can be realized by different methods such as chemical vapor transport, molecular beam epitaxy, and electrodeposition. The last method is used in the present work allowing the growth of structures such as p-n junctions, intercalation of magnetic or superconducting dots. We report the synthesis of high-quality TI NW: Bi_2Te_3, Sb_2Te_3 and p-n junction via electrodeposition. Structural, morphological, and nanostructure properties of NWs have been investigated by various characterization techniques. Interface structures and lateral heterojunctions (LHJ) in p-n junction NWs has also been made.

INTRODUCTION

Discovery of new class of materials named topological insulator (TIs) initiated intense research motivated by the novel physical properties of TIs and perspectives for device applications in spintronics and quantum computation processing [Hasan and Kane, 2010; Hasan and Moore, 2011; Luo et al., 2013; Le et al., 2014; Tu et al., 2015]. Electronic band structure of those materials is fully gapped in the bulk, but with unusual gapless 'protected' 2D Dirac surface state [Liu et al., 2019; Moore, 2010; Qi and Zhang, 2011]. This band structure arises in compounds containing high atomic mass elements with strong spin-orbit coupling. This prediction was followed by several experiments, angular-resolved photoemission spectroscopy and scanning tunneling microscopy demonstrating locked spins [Alpichshev et al., 2010; Chen et al., 2009; Hsieh et al., 2009; Wang et al., 2011; Zhang et al., 2009].

The presence of topologically protected and spin-locked surface states inhibits backscattering and leads to very long dephasing lengths. These systems could be promising in the field of spintronics and fault-tolerant quantum computing. However, access to this 2D quantum matter is a challenge, due to the difficulty of separating surface contributions from the non-conductivity of the bulk. In approaches taken thus far, such as nanostructured synthesis/growth, doping, compositional tuning, or band gap engineering via device gating, complete suppression of the bulk conduction in TIs has not yet been realized. Existence of Dirac cone type surface states was found in several systems, and one can distinguish several classes of TIs. Time reversal symmetry protected family represented by layered Bi_2Te_3, Bi_2Se_3, Sb_2Te_3, and crystal symmetry protected, cubic $Pb_{1-x}Sn_xSe$, SnTe, and Kondo type SmB_6.

Electronic transport properties specific to the surface conduction channel are difficult to separate from bulk conductivity. In most cases, linear in field magneto resistance due to weak anti-localization and Berry phase in Shubnikov-de Hass oscillations are observed on the large background. This jeopardizes verification of theoretical predictions of novel quantum effects such as Majorana fermions on the interface among TI and superconductor, Klein tunneling and Mach-Zehnder interferometer on TI-based p-n junction. The main obstacle is the fabrication of high-quality TI materials and structures.

Nano scale TI has a large surface-to-volume ratio that can manifest the conductive surface states and are promising candidates for devices [Guo et al., 2015; Hong et al., 2014; Ilan et al., 2015; Kong et al., 2010.]. There are number of studies focused on the fabrication and characterization of thin-films and nanoplates

[1]Laboratoire des Solides Irradiés, UMR 7642 CEA-CNRS-Ecole polytechnique, France

[2]Laboratoire de Physique de la Matière Condensée, UMR 7643 CNRS-Ecole polytechnique, France

[3]Lead contact

*Correspondence: newton_rashmi51@yahoo.com

https://doi.org/10.1016/j.isci.2021.102694

[Fein et al., 2015; Jiang et al., 2015; Le et al., 2017; Zhang et al., 2012.], much less attention has been given to the TIs nanostructured such as nanowires (NWs), nanorods, and nanotubes [Eschbach et al., 2015; Krieg et al., 2019; Zuev et al., 2010.]. Three different technological methods are commonly used to produce TI NWs: photolithography, vapor transport with seed and template electrodeposition growth. The last approach offers a less expensive and convenient way to fabricate periodically aligned NWs with uniform diameter which is very useful for nanostructured electronic applications [Pinisetty et al., 2011]. It also has considerable advantages over other methods in fabrication of complex heterostructures such as p-n junctions, interfaces with magnetic or superconducting materials, although no systematic study of the layered structure (Sb_2Te_3/Bi_2Te_3) in p-n junction TIs NWs has been performed.

In this article, we present a convenient method to fabricate the p-n junction TIs NWs with defect-free interface by electrodeposition. We also discuss on comparative studies of structural and morphological properties of Bi_2Te_3, Sb_2Te_3 and p-n junction TIs NWs. We believe that our results add a new approach for further study of interface structure in p-n junction NW. To the best of our knowledge, this is the first report on the lateral heterojunction (LHJ) in Sb_2Te_3/Bi_2Te_3 p-n junction TIs NW.

RESULTS AND DISCUSSIONS

Nano structural analysis of Bi_2Te_3, Sb_2Te_3 and p-n junction NWs

X-ray diffraction (XRD) patterns of Bi_2Te_3, Sb_2Te_3 and p-n junction TIs NWs embedded in polycarbonate template [Figures S1A–S1C] show diffraction peaks of all the three samples correspond to the rhombohedral phase with R3 space group of Bi_2Te_3 (JCPDS card: 00-015-0863), Sb_2Te_3 (JCPDS: 00- 015–0874) and p-n junction. The peaks from gold (JCPDS card 00-04-0784) are clearly observed. The peak around $2\theta \sim 17.2^0$ (shown by *) corresponds to two peaks, one from the sample and other from the polycarbonate membrane; so we decided to focus our analysis only on pure peaks of the samples. XRD patterns of Bi_2Te_3 [Figure S1A] and Sb_2Te_3 [Figure S1B] are mostly similar, and there is no trace of any secondary phase was found although broadening in the background has been detected for Sb_2Te_3 NWs which could be attributed to amorphous phase or poor crystallinity exist in the antimony telluride. The peak (015) for both samples Bi_2Te_3 and Sb_2Te_3, indicating a highly preferential orientation of the NWs along the [015] direction and the same orientation maintained in the p-n junction NWs [Figure S1C]. Figure 1A shows the comparison of XRD of three samples. In Figure 1B clearly the strong peaks (015) of both Sb_2Te_3 and Bi_2Te_3 are well observed in the p-n junction, indicating the nice phase separation in the sample. However, a small shift of peaks has been found $\sim 0.03^0$ which is small enough to consider error bar in XRD analysis. Figure 1C depicts that all observed peaks of Bi_2Te_3 and Sb_2Te_3 are present in p-n junction which indicating bimetal structure. In addition, we noticed that the peaks oriented in (110) are broader than the peak (015) indicating a smaller crystallite size or a greater lattice strain more effective in [110] direction. To investigate the lattice strain and crystallite size of the wires, we followed the procedure recommended by Langford [Langford and Wilson, 1978]. Here we used the Halder-Wagner plots for analyzing the crystallite size (Dv) and microstrain (ε) of the wires (discussed in next section microstructure analysis). Figure 1D clearly shows, for each of the three samples, that the points are aligned along a line without y-intercept (or very small value), indicating that the broadening is mainly due to a crystallite size effect. In that case, the Scherrer formula can also be used to extract the average crystallite size, according to the well-known formula:

$$\beta = K\,\lambda / (D\cos\theta)$$

where K = 1.0747 is the Scherrer's constant (in the case of the use of integral breadth (β) to characterize the broadening). It can be seen that the calculated value of crystallite size agreed well with the two approaches [Table 1] and an anisotropy in size is observed on Halder-Wagner plots. Considering the weak intensities of the peaks, the calculated crystallite sizes should be taken as tendency instead of absolute values, while the average value ~30 nm is well corresponded with the diameter of the polycarbonate membrane.

Moving now to explaining the morphology and crystallinity of the Bi_2Te_3, Sb_3Te_3 and p-n junction NWs. Figures 2A–2F which clearly display the uniformity in morphology with the smooth surface for all the three samples which makes them good candidate for future fabrication of a nanostructured devices. High-resolution transmission electron microscopy (TEM) and selected area electron diffraction (SAED) patterns with shiny fringes [Figure S2 (A) and S3] for Bi_2Te_3 shows a good crystallinity and can be indexed to the rhombohedral crystal structure (JCPDS card no. (15–0863) with the lattice spacing of the shell is 1.49 Å corresponding to the [1115] plane which is in good agreement with XRD. On the contrary for the antimony

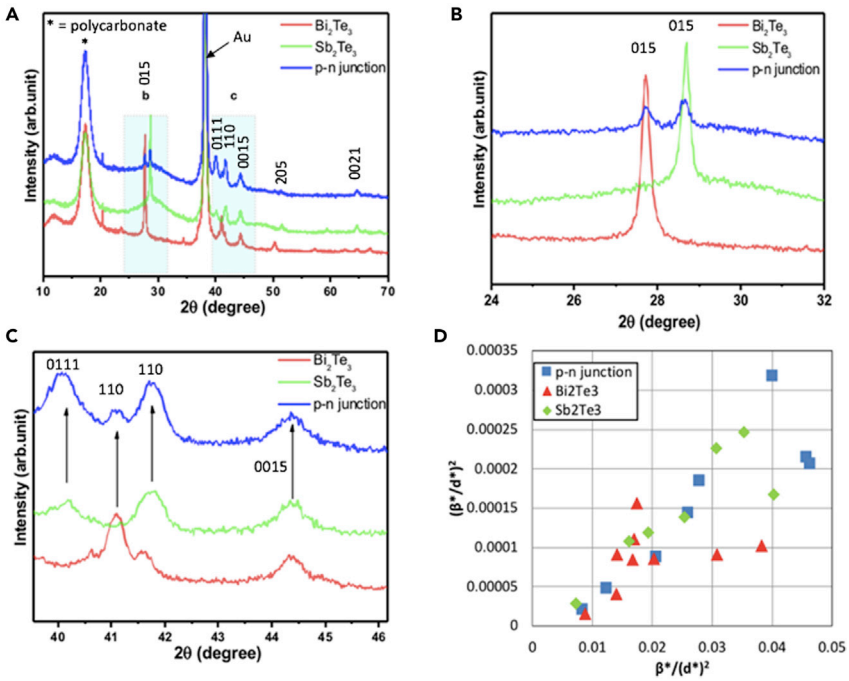

Figure 1. X-ray diffraction patterns of Bi_2Te_3, Sb_2Te_3 and p-n junction NWs imbedded in polycarbonate

(A) Combined XRD graph of Bi_2Te_3, Sb_2Te_3, and p-n junction NWs imbedded in polycarbonate membrane note that the peaks at ~ 17° and ~38° correspond to the polymer and gold, respectively. Two areas (blue) between 24 and 30° and 40-46° 2θ is taken for zoom graph for clear visibility of the peaks of each three samples

(B and C) Zoom graph of Bi_2Te_3, Sb_2Te_3 and p-n junction NWs in the range 24–32° 2θ showing peak orientation (B) in the range 40–46° 2θ(C).

(D) Halder-Wagner plots used to microstrain analysis in the Bi_2Te_3, Sb_2Te_3 and p-n junction NWs.

telluride, we found that most of the NWs are completely amorphous [Figure S4D], while few of them are the mixture of amorphous and crystalline phase [Figure S4E]. Notably crystalline phase corresponds to the rhombohedral crystal structure (JCPDS card no. [15–0874]) with the lattice spacing of the shell is 3.29 Å corresponding to the [015] plane which matches with the most intense peak of XRD [Figure S1B]. Through careful investigation, as discussed in later section (Structural and chemical analysis of antimony telluride), amorphous phase was also found in XRD although crystalline phase was well observed with pure intense peaks which arouses the fact that crystalline phase could be improved and possibly antimony telluride could be maintain the layered structure in p-n junction and provide us with the opportunity to further investigate their electronic properties through this structure.

Microstructure analysis

The recommended procedure

Computing the integral breath (IB) and the full with at half maximum (FWHM) of a pseudo-Voigt curve from the broadened profile to obtain the shape factor (Q = FWHM/IB), calculating the breadths of the constituent profiles corrected for instrumental broadening (using NIST LaB6 standard to determine the instrumental broadening using the Caglioti function) and analyzing the Williamson-Hall and Halder-Wagner

Table 1. Microstructural analysis for the Bi_2Te_3, Sb_2Te_3 and p-n junction. Dv(HW) and Dv(S) for volume-weighted average crystallite sizes from Halder-Wagner and Scherrer formalisms, respectively.

Samples		Dv (HW) (nm)	ε (r.m.s.)	Dv (S) (nm)
Sb_2Te_3		24	0.0037	20
Bi_2Te_3		33	0	30
p-n junction	Bi_2Te_3	23	0	22
	Sb_2Te_3	30	0	30

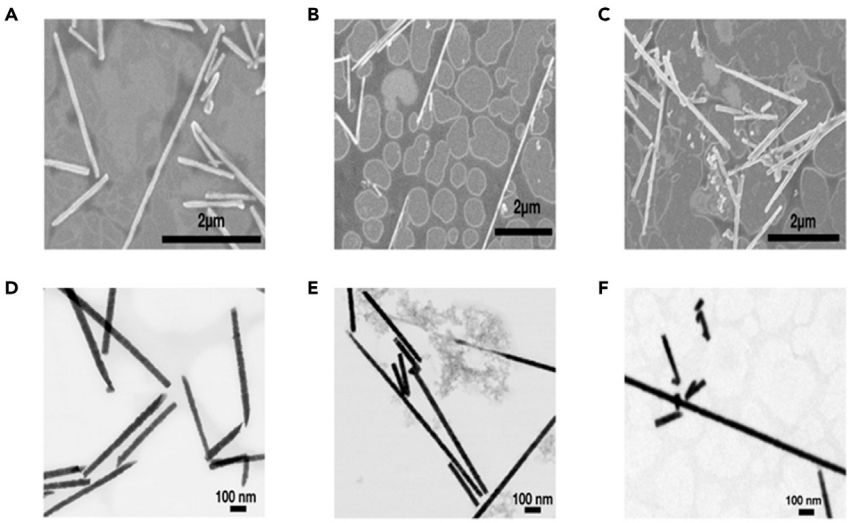

Figure 2. SEM and STEM -BF image of Bi_2Te_3 NWs (a), Sb_2Te_3 NWs (b) and p-n junction NWs

(A–C) SEM image of Bi_2Te_3 NWs (A), Sb_2Te_3 NWs (B), and p-n junction NWs (C) on silicon wafer after dissolving the polycarbonate membrane in CH_2Cl_2 solution.

(D–F) STEM-BF images of Bi_2Te_3 NWs (D), Sb_2Te_3 NWs (E), and p-n junction NWs (F) on carbon grid after dissolving the polycarbonate membrane in CH_2Cl_2 solution.

plots [Izumi and Ikeda, 2004]. These plots are a very useful overview of the microstructural properties of the sample, highlighting possible anisotropic behavior according to (hkl) planes and giving an approximate values of the crystallite size Dv (volume-weighted average size) and microstrain ε (r.m.s) for root-mean-square of the variation in the lattice parameter due to the effect of several defects.

The well-known Williamson-Hall plot follows the equation:

$$\beta\cos\theta / \lambda = C\varepsilon \sin\theta / \lambda + K/D \qquad \text{(Equation 1)}$$

A slope close to zero indicates that the broadening is due to crystallite size effect only, with crystallites exhibiting an average spherical shape. C = 2 and K = 4/3 are recommended by Izumi et al., assuming the hypothesis of a spherical crystallite shape [Ida et al., 2003].

When this approach is used with Lorentzian peak shape, a negative microstrain can be obtained that is not physically meaningful. For the determination of Dv and ε, Halder and Wagner [Halder and Wagner, 1966] proposed an alternative equation adapted for $0.663662 < \phi < 0.93949$ corresponding to the pseudo-voigt function containing the integral breadth, β^* of the reciprocal lattice point ($\beta^* = \beta\cos\theta/\lambda$) and the lattice plane spacing, d^* for the reciprocal cell ($d^* = 2\sin\theta/\lambda$) as:

$$(\beta^* / d^*)^2 = K/D.\ \beta^* / (d^*)^2 + (2\varepsilon)^2 \qquad \text{(Equation 2)}$$

The value of K = 4/3 is believed to be valid for the size (as the volume-weighted average) of spherical crystallites [Langford and Wilson, 1978]. This equation does not contain the constant C, for which the value is still under discussion. As our factors were calculated between ($\phi < 0.63662$), we selected HW method for our study.

Structural and chemical analysis of antimony telluride

In this study, we have analyzed the structure and the chemical composition of antimony telluride (Sb_2Te_3) NWs by using XRD and TEM.

Figure S1B shows the XRD of Sb_2Te_3 NWs imbedded in polycarbonate membrane. We can see the well-defined peaks, corresponding to the crystalline phase (JCPDS 15–0874) except the broadening in background. This may be due to the polycarbonate membrane [Figure S4B], but by careful investigation we

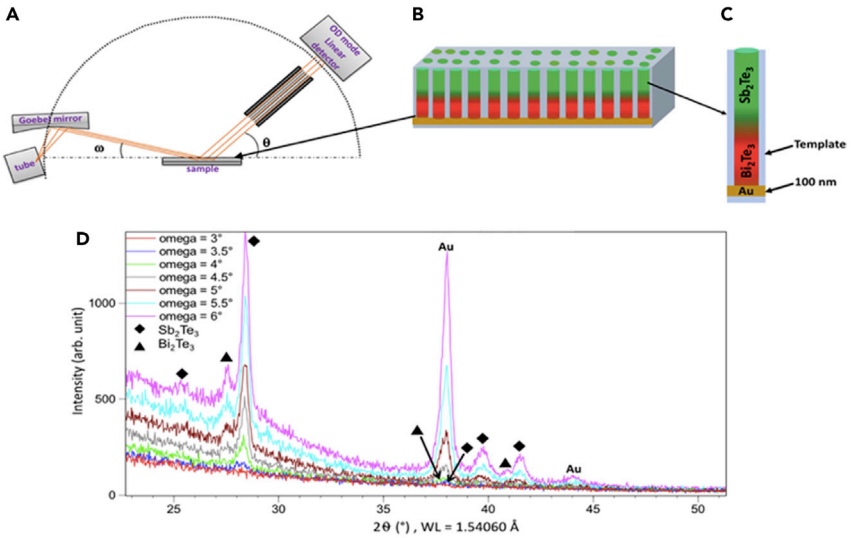

Figure 3. GIXRD of p-n junction NWs

(A) Diagram showing the technique of GIXRD used for Bilayer structure measurement in p-n junction NWs.

(B) model displaying growth of p-n junction NWs inside the membrane.

(C) Sketch of individual single p-n junction NW.

(D) GIXRD of p-n junction NWs indicating layer structure correspond to Bi_2Te_3 and Sb_2Te_3. Incidence angles (ω) taken from 3° to 6°.

detected the broadening in the base of the main peak (015) which is due to the sample [Figure S4A, inset Figure S4B], and it can be explained by the existence of amorphous phase in the antimony telluride. Furthermore, the composition difference between index Sb_2Te_3 and sample observed is confirmed by EDX [Figure S4C] which indicates a stoichiometry of the sample nearly Sb_3Te.

With SAED and HRTEM, we can see that the majority of antimony telluride NWs is amorphous [Figures S4D and S4E]. Nevertheless, a few NWs are crystalline in the core, as can be seen in [Figure S4E]. This crystalline phase corresponds to Sb_2Te_3 phase (JCPDS 17–0874). Some reports said that at room temperature it is common to find noncrystalline/amorphous structure for Sb_2Te_3 which can be transformed to the crystalline structure by the annealing [Kim and Oh, 2010]. It has also been reported that it is difficult to synthesize compositionally controlled crystalline Sb_2Te_3 by electrodeposition [Lensch-Falk et al., 2012].

Overall XRD and TEM experiments bring out the presence of both amorphous and crystalline phases in antimony telluride NWs; however crystalline phase was dominated in XRD. It has been also observed stoichiometric defects or impure phase in the antimony telluride which is quite common for electrodeposition due to deposition potential and it could be improve during the deposition. Since the electrodeposition was carried out at the room temperature which could be the reason for amorphous phases in antimony telluride NWs.

Layer structured p-n junction NWs analysis

Grazing incidence-XRD (GIXRD) technique was used to study the layer of Sb_2Te_3 and Bi_2Te_3 in p-n junction NW represented systematically in Figure 3A [see in supplemental information, Figures S5A and S5B]. The p-n junction sample was made to obtain a layered structure as depicted in Figures 3B and 3C. In this experiment, we use grazing angle (ω) starting from 3° to 6° to see the layer structure in the p-n junction, Figure 3D. At $\omega = 4°$, we clearly observed the peaks only for Sb_2Te_3: (PDF 15–0874), indicating the first layer of the p-n junction [Figure S6A]. The peaks for Bi_2Te_3 (PDF 15–0683) have been found when (ω) is increasing up to 5° [Figure S6B]. Once (ω) reached 7°, GIXRD shows peaks for gold (PDF 65–2870) that defines surface of the substrate [Figure S6C]. Interestingly, we can see that the crystal structure of Sb_2Te_3 and Bi_2Te_3 in p-n junction remain the same as the pure phase, indicating that formation of p-n junction does not lead to the formation of a ternary phase made by Sb_2Te_3 and Bi_2Te_3. No evidence of solid solution was detected in the p-n junction, which may explain the abrupt interface between p and n-type.

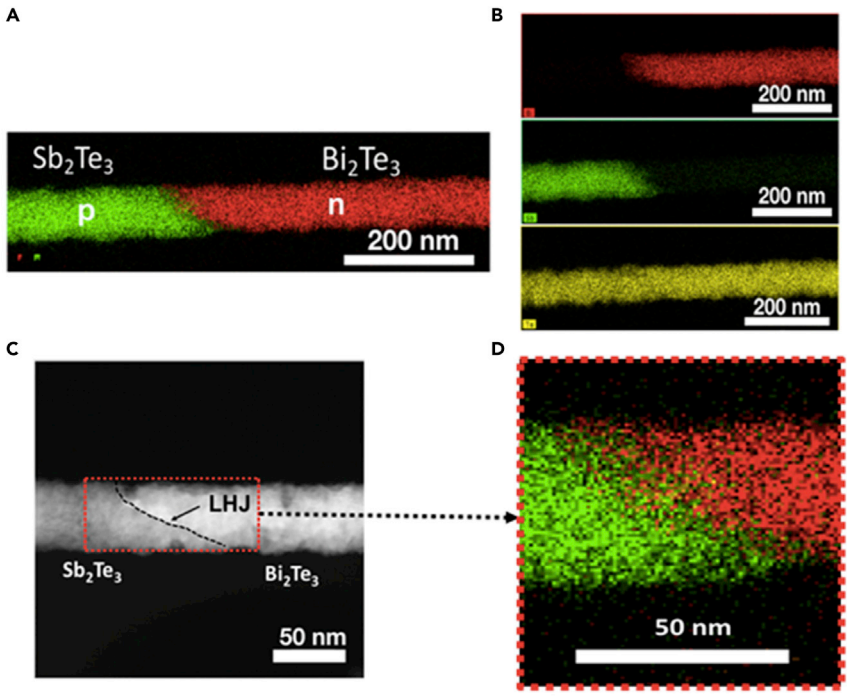

Figure 4. Elemental mapping of p-n junction NW

(A) Elemental mapping of the p-n junction single NW on carbon grid showing two components Sb_2Te_3 and Bi_2Te_3, respectively, in single NW.

(B) Bi (shown red), Sb (shown green), and Te (shown yellow) contents of the p-n junction NW.

(C) Lateral heterojunction (LHJ) identified in transition region in single p-n junction NW showing junction is abrupt (showed by black dotted line).

(D) Enlarge image of the interface in p-n junction NW.

To investigate the interface structure in p-n junction NWs, we performed STEM. Figure 4A depicts an elemental mapping by EDX of the p-n junction. STEM measurement reveals that the NW has two compounds: Sb_2Te_2 and Bi_2Te_3 which respectively correspond to p and n types layered structure in p-n junction NW. Figure 4B shows the homogeneous spatial distribution of the Biand Sb elements in the p-n junction NW, as well as the presence of Te throughout the whole wire. The two contrast dark and bright were, respectively, found to be composed of Sb_2Te_3 and Bi_2Te_3 in Figure 4C due to the difference of the mean atomic numbers of both regions. This contrast change is also observed in boundary of the NW which implies the loss of resolution at the edge of the wire [Fang et al., 2013]. Notably, existence of LHJ (Sb_2Te_3/Bi_2Te_3) in transition region has been observed (shown by dotted line) which was also reported by [Fein et al., 2015]. In TI physics LHJs play a more interesting role than vertical ones because new interface state generated between two SS region in the same plane [Hasan and Kane, 2010; Ilan et al., 2015]. Additionally, we can see the explicit interface of the lateral layers (Sb_2Te_3/Bi_2Te_3) in p-n junction which proves that our strategy to control over the mixture between two layers in transition region during the synthesis by deposing the amount of initial precursor is quite successful.

The STEM of the p-n junction gives additional information on the interface. First, STEM-HAADF imaging brings out the fact that the transition between bismuth telluride and antimony telluride is sharp from a chemical point of view, clearly evidenced by the difference in contrast between the n and the p types regions. Second, we can see that this slantwise interface is not flat and presents some rugosity from one side of the NW to the other. This is clearly evidenced by the STEM-HAADF imaging and can explain the origin of the apparent Biand Sb intermixing on the STEM-EDX mapping Figure 4D.

p-n junction NWs synthesis for electronic application

According to requirement of the electronic applications, we used AAO porous membrane for getting long and perfectly cylindrical NWs, and we performed SEM to investigate influences of AAO membrane on the

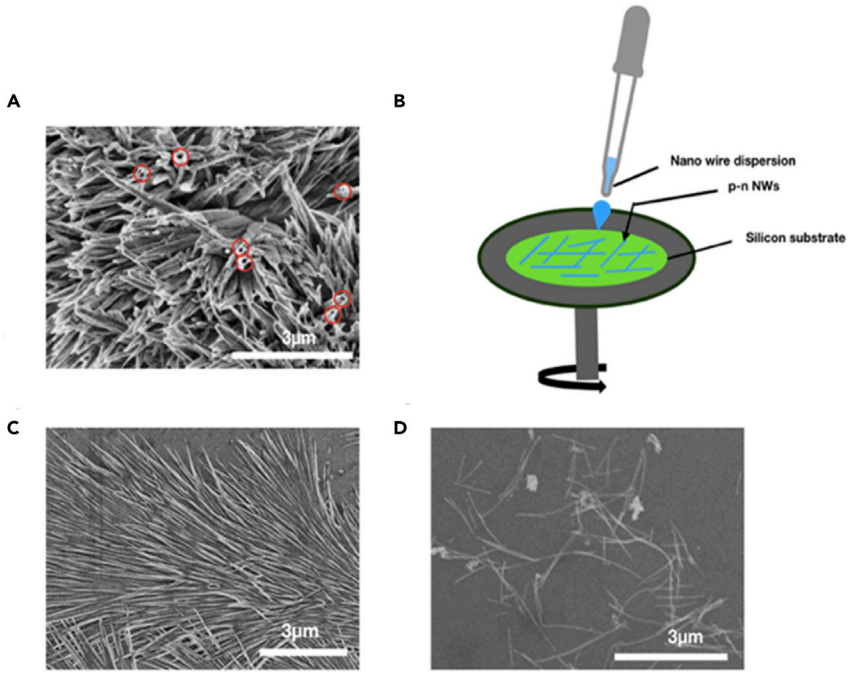

Figure 5. Systematic diagram of dispersing p-n junction NWs by spin-coating technique

(A) Top view SEM image of p-n junction NWs spreading on silicon wafer after dissolving AAO membrane in NaOH

(B) Systematic diagram of spin-coating technique used for dispersing NWs for electronic application.

(C and D) SEM image of p-n junction NWs after using spin coating at speed 1000 rpm (C) and at speed 2000 rpm (D).

growth of the NWs. [Figure S7] depict that the p-n junction NWs with large quantity obtained after dissolving the membrane illustrate the NWs with smooth contours and have a narrow size distribution with a diameter around 80 nm as expected. The length of the NWs ranges tens of microns to few millimeters, suggesting that the 100% growth of NWs. Figure 5A shows the top view of the p-n junction NWs after dissolving the template in aqueous NaOH solution. Only a few pores remain blank. The filling ratio is quite higher than the porosity of the template. To get single dispersed p-n junction NW for further application followed by lithography, we used spin-coating technique (depicted as Figure 5B). Concentrated p-n NW suspension in ethanol was diluted by about one thousand times. The suspension was the deposited on to the silicon wafer by spin coating at the rotatory speed of 1000 rpm. It can be noted that uniform distribution of NWs has been obtained Figure 5C may be due to the balance between centrifugal force and viscous force of the liquid in the spin-coating process [Xie et al., 2013]. When we increased the rotatory speed to 2000 rpm Figure 5D interestingly a unique morphology of the p-n junction NWs is discovered which are referred to as zigzag NWs. It may be due to the viscous force which is lower that centrifugal force due to the high rotatory speed. It has also been reported that the appearance of zigzag morphologies comes from the partially low surface-interfacial energy on the surface of the droplets [Park and Lee, 2014]. Some other reports show that low surface-interfacial energy break the continuous straight growth of NWs [Ma et al., 2004; Moore and Balents, 2007]. This cause some p-n NWs break into small pieces but still some of them have length of 5–7 μm which could be used for applications. Since NWs are completely detached with one another they shall be used for four probe measurements followed by photo lithography which is the object of a forthcoming publication.

Conclusions

In conclusion, we explored the comparative analysis of structural and morphological properties of Bi_2Te_3, Sb_2Te_3 and p-n junction NWs. We have demonstrated for the first time a template-based growth strategy for the synthesis of heterostructure (Sb_2Te_3/Bi_2Te_3) p-n junction NWs, using electrodeposition as the synthesis method. We have also described the layer structure in p-n junction NWs by GIXRD technique. Stem reveals several important points; first, p-n junction has two compositions p and n type; second, existence of LHJ in the transition region has been identified; third, sharp interface about $\leq$10 nm has been explored

which was observed first time in electrodeposition template growth. Thus, we believe that the growth of the p-n NWs with explicit interface would have profound potential for offering a promising building block for next generation spintronics devices. Spin-coating technique has applied for dispersing p-n junction NWs and finding individual one would be interesting for further potential applications.

LIMITATIONS OF THE STUDY

The spin-coating technique is being improved to get single dispersed NW for electrical measurements followed by lithography. Therefore electrical properties of the p-n junction NW will have to be further evaluated.

STAR★METHODS

Detailed methods are provided in the online version of this paper and include the following:

- KEY RESOURCE TABLE
- RESOURCE AVAILABILITY
  - Lead contact
  - Materials availability
  - Data and code availability
- METHOD DETAILS
  - Materials
  - Synthesis of Bi_2Te_3, Sb_2Te_3 and p-n junction NWs
  - Electrodeposition of Bi_2Te_3, Sb_2Te_3 and p-n junction NWs
  - Characterizations

SUPPLEMENTAL INFORMATION

Supplemental information can be found online at https://doi.org/10.1016/j.isci.2021.102694.

ACKNOWLEDGMENTS

The authors are grateful to the Ecole Polytechnique for financing the postdoctoral of Rashmi Rani.

AUTHOR CONTRIBUTIONS

The authors have contributed equally.

DECLARATION OF INTERESTS

The authors declare no competing interests.

Received: February 1, 2021
Revised: May 24, 2021
Accepted: June 3, 2021
Published: June 25, 2021

REFERENCES

Alpichshev, Z., Analytis, J.G., Chu, J.H., Fisher, I.R., Chen, Y.L., Shen, Z.X., Fang, A., and Kapitulnik, A. (2010). STM imaging of electronic waves on the surface of Bi2Te3: topologically protected surface states and hexagonal warping effects. Phys. Rev. Lett. *104*, 016401–016405. https://doi.org/10.1103/PhysRevLett.104.016401.

Chen, Y.L., Analytis, J.G., Chu, J.H., Liu, Z.K., Mo, S.K., Qi, X.L., Zhang, H.J., Lu, D.H., Dai, X., Fang, Z., et al. (2009). Experimental realization of a three-dimensional topological insulator, Bi_2Te_3. Science *325*, 178–181. https://doi.org/10.1126/science.1173034.

Eschbach, M., Mlynczak, E., Kellner, J., Kampmeier, J., Lanius, M., Neumann, E., Weyrich, C., Gehlmann, M., Gospodari, P., Dring, S., et al. (2015). Realization of a vertical topological p–n junction in epitaxial Sb_2Te_3/Bi_2Te_3 heterostructures. Nat. Commun. *6*, 8816–8817. https://doi.org/10.1038/ncomms9816.

Fang, H., Feng, T., Yang, H., Ruan, X., and Wu, Y. (2013). Synthesis and thermoelectric properties of compositional-modulated lead telluride–bismuth telluride nanowire heterostructure. Nano Lett. *13*, 2058–2063. https://doi.org/10.1021/nl400319u.

Fein, F., Wei, Z., Wang, Q., Lu, P., Wang, S., Qin, Y., Pan, D., Zhao, B., Wang, X., Sun, J., et al. (2015). Solvothermal synthesis of lateral heterojunction Sb2Te3/Bi2Te3 nanoplates. Nano Lett. *15*, 5905–5911. https://doi.org/10.1021/acs.nanolett.5b01987.

Grazulis, S., Chateigner, D., Downs, R.T., Yokochi, A.F.T., Quirats, M., Lutterotti, L., Manakova, E., Butkus, J., Moeck, P., and Bail, A. Le. (2009). Crystallography Open Database – an-open-access collection of crystal structures. J. Appl. Cryst. *42*, 726–729. https://doi.org/10.1107/S0021889809016690.

Guo, Y., Li, Z., and Peng, H. (2015). A roadmap for controlled production of topological insulator nanostructures and thin films. Small *11*, 3290–3305. https://doi.org/10.1002/smll.201403426.

Halder, N.C., and Wagner, C.N.J. (1966). Separation of particle size and lattice strain in integral breadth measurements. Acta Cryst. *20*, 312–313. https://doi.org/10.1107/S0365110X66000628.

Hasan, M.Z., and Kane, C.L. (2010). Colloquium: topological insulators. Rev. Mod. Phys. *82*, 3045–3067. https://doi.org/10.1103/RevModPhys.82.3045.

Hasan, M.Z., and Moore, J.E. (2011). Three-dimensional topological insulators. Annu. Rev. Condens. Matter Phys. *2*, 55–78. https://doi.org/10.1146/annurev-conmatphys-062910-140432.

Hong, S.S., Zhang, Y., Cha, J.J., Qi, X.L., and Cui, Y. (2014). One-dimensional helical transport in topological insulator nanowire interferometers. Nano Lett. *14*, 2815–2821. https://doi.org/10.1021/nl500822g.

Hsieh, D., Xia, Y., Qian, D., Wray, L., Meier, F., Dil, J.H., Osterwalder, J., Patthey, L., Fedorov, A.V., Lin, H., et al. (2009). Observation of time-reversal-protecte single-Dirac-ConeTopological-Insulator states in Bi_2Te_3 and Sb_2Ti_3. Phys. Rev. Lett. *103*, 146401–146404. https://doi.org/10.1103/PhysRevLett.103.146401.

Ida, T., Shimazaka, S., Hibino, H., and Toraya, H. (2003). Diffraction peak profiles from spherical crystallites with lognormal size distribution. J.Appl. Cryst. *36*, 1107–1115. https://doi.org/10.1103/PhysRevLett.115.096802.

Ilan, R., Juan, F.D., and Moore, J.E. (2015). Spin-based mach-zehnder interferometry in topological insulator p-n junctions. Phys. Rev. Lett. *115*, 096802–096805. https://doi.org/10.1103/PhysRevLett.115.096802.

Izumi, F., and Ikeda, T. (2004). Advance ceramic research centre Annual report. 3, 33-38.

Jiang, X., Zhang, X., Wang, Y., Wang, N., West, D., Zhang, S., and Zhang, Z. (2015). Tunable GaTe- MoS2 van der Waals p-n junctions with novel optoelectronic performance. Nano Lett. *15*, 3147–3152. https://doi.org/10.1021/acs.nanolett.5b03291.

Kim, M.-Y., and Oh, T.-S. (2010). Crystallization behavior and thermoelectric characteristics of the electrodeposited Sb2Te3 thin films. Thin Solid Films *518*, 6550–6553. https://doi.org/10.1016/j.tsf.2010.03.052.

Kong, D., Randel, J.C., Peng, H., Cha, J.J., Meister, S., Lai, K., and Chen, Y. (2010). Topological insulator nanowires and nanoribbons. Nano Lett. *10*, 329–333. https://doi.org/10.1021/nl903663a.

Krieg, J., Giraud, R., Funke, H., Dufouleur, J., Escoffier, W., Trautmann, C., and Toimil-Molares, M.E. (2019). Magnetotransport measurements on Bi2Te3nanowires electrodeposited in etched ion-track membranes. J. Phys. Chem. Sol. *128*, 360–366. https://doi.org/10.1016/j.jpcs.2018.02.002.

Langford, J.I., and Wilson, A.J.C. (1978). Scherrer after sixty years: a survey and some new results in the determination of crystallite size. J.Appl. Cryst. *11*, 102–113. https://doi.org/10.1107/S0021889878012844.

Le, P.H., Tzeng, W.Y., Chen, H.J., Luo, C.W., Lin, J.Y., and Leu, J. (2014). Superconductivity in textured Bi clusters/Bi_2Te_3 films. APL Mater. *2*, 096105–096107. https://doi.org/10.1063/1.4894779.

Le, P.H., Liu, P.T., Luo, C.W., Lin, J.Y., and Wu, K.H. (2017). Thickness-dependent magnetotransport properties and terahertz response of topological insulator Bi2Te3 thin films. J. Alloys Comps. *692*, 972–979. https://doi.org/10.1063/1.4894779.

Lensch-Falk, J.L., Banga, D., Hopkins, P.E., Robinson, D.B., Stavila, V., Sharma, P.A., and Medlin, D.L. (2012). Electrodeposition and characterization of nano-crystalline antimony telluride thinfilms. Thin Solid Films *520*, 6109–6117. https://doi.org/10.1016/j.tsf.2012.05.078.

Liu, P., Willian, J.R., and Cha, J.J.((2019). Topological nanomaterials. Nat. Rev. Mater. *4*, 479–496. https://doi.org/10.1038/s41578-019-0113-4.

Luo, C.W., Wang, H.J., Ku, S.A., Chen, H.J., Yeh, T.T., Lin, J.Y., Wu, K.H., Juang, J.Y., Young, B.L., Kobayashi, T., et al. (2013). Snapshots of Dirac fermions near the Dirac point in topological insulators. Nano Lett. *13*, 5797–5802. https://doi.org/10.1021/nl4021842.

Ma, C., Ding, Y., Moore, D., Wang, X.D., and Wang, Z.L. (2004). Single-crystal CdSe nanosaws. J. Am. Chem. Soc. *126*, 708–709. https://doi.org/10.1021/ja0395644.

Moore, J.E., and Balents, L. (2007). Topological invariants of time-reversal-invariant band structures. Phys. Rev. B. *75*, 121306–121314. https://doi.org/10.1103/PhysRevB.75.121306.

Moore, J.E. (2010). The birth of topological insulators. Nature *464*, 194–198. https://doi.org/10.1038/nature08916.

Park, Y.S., and Lee, J.S. (2014). Synthesis of single-crystalline topological insulator Bi_2Se_3 nanomaterials with various morphologies. J. Nanoparticle Res. *16*, 2226–2227. https://doi.org/10.1007/s11051-013-2226-9.

Pinisetty, D., Gupta, M., Karki, A.B., Young, D.P., and Devireddy, R.V.J. (2011). Fabrication and characterization of electrodeposited antimony telluride crystalline nanowires and nanotubes. J. Mater. Chem. *21*, 4098–4107. https://doi.org/10.1039/C0JM01969K.

Qi, X.L., and Zhang, S.C. (2011). Topological insulators and superconductors. Rev. Mod. Phys. *83*, 1057–1110. https://doi.org/10.1103/RevModPhys.83.1057.

Tu, C.M., Yeh, T.T., Tzeng, W.Y., Chen, Y.R., Chen, H.J., Ku, S.A., Luo, C.W., Lin, J.Y., Wu, K.H., Juang, J.Y., et al. (2015). Manifestation of a second Dirac surface state and bulk bands in THz radiation from topological insulators. Sci. Rep. *5*, 14128–14136. https://doi.org/10.1038/srep14128.

Wade, T.L., and Wegrowe, J.-E. (2005). Template synthesis of nanomaterials. Eur. Phys. J. Appl. Phys. *29*, 3–22. https://doi.org/10.1051/epjap:2005001.

Wang, G., Zhu, X.G., Sun, Y.Y., Li, Y.Y., Zhang, T., Wen, J., Chen, X., He, K., Wang, L.L., Ma, X.C., et al. (2011). Topological insulator thin films of Bi_2Te_3 with controlled electronic structure. Adv. Mater. *23*, 2929–2932. https://doi.org/10.1002/adma.201100678.

Xie, S., Ouyang, Z., Jia, B., and Gu, M. (2013). Large-size, high-uniformity, random silver nanowire networks as transparent electrodes for crystalline silicon wafer solar cells. Opt. Express *21*, 355–362. https://doi.org/10.1364/OE.21.00A355.

Zhang, T., Cheng, P., Chen, X., Jia, J.F., Ma, X., He, K., Wang, L., Zhang, H., Dai, X., Fang, Z., et al. (2009). Experimental demonstration of topological surface states protected by time-reversal symmetry. Phys. Rev. Lett. *103*, 266803–266804. https://doi.org/10.1103/PhysRevLett.103.266803.

Zhang, Y., Snedaker, M.L., Birkel, C.S., Mubeen, S., Ji, X., Shi, Y., Liu, D., Liu, X., Moskovits, M., and Stucky, G.D. (2012). Silver-based intermetallic heterostructures in Sb2Te3 thick films with enhanced thermoelectric power factors. Nano Lett. *12*, 1075–1080. https://doi.org/10.1021/nl204346g.

Zuev, Y.M., Lee, J.S., Galloy, C., Park, H., and Kim, P. (2010). Diameter dependence of the transport properties of antimony telluride nanowires. Nano Lett. *10*, 3037–3040. https://doi.org/10.1021/nl101505q.

STAR★METHODS

KEY RESOURCE TABLE

REAGENT or RESOURCE	SOURCE	IDENTIFIER
Chemicals, peptides, and recombinant proteins		
Bismuth nitrate	Sigma Aldrich chemicals, USA	CAS Number 10035-06-0
Antimony chloride	Sigma Aldrich chemicals, USA	CAS Number 10025-91-9
Tellurium oxide	Sigma Aldrich chemicals, USA	CAS Number 7446-07-3
Nitric acid	Sigma Aldrich chemicals, USA	CAS Number 7696-37-2
Sodium hydroxde	Sigma Aldrich chemicals, USA	CAS Number 1310-73-2
Acetone	VWR	CAS Number 67-64-1
Ethanol	VWR	CAS Number 64-17-5
Deposited data		
Bi_2Te_3 - crystal structure	This paper	JCPDS card: 00-015-0863
Sb_2Te_3- crystal structure	This paper	JCPDS card: 00- 015-0874
Membrane		
Anodic aluminum oxide	InRedox	CAS Number 1344-28-1
Polycarbonate membrane	Millipore Sigma	Catalog number DTTP04700

RESOURCE AVAILABILITY

Lead contact

Further information and requests for resources and materials should be directed to and will be fulfilled by the Lead Contact, Rashmi Rani (newton_rashmi51@yahoo.com).

Materials availability

This study did not generate new unique reagents.

Data and code availability

There is no dataset or code associated with this work.

METHOD DETAILS

Materials

Bismuth nitrate ($Bi(N0_3)_3{\cdot}5H_20$, 99.997%, Sigma Aldrich chemicals, USA), Antimony chloride ($SbCl_3$, 99.997%, Sigma Aldrich chemicals, USA), Tellurium oxide (TeO_2, 99.997%, Sigma Aldrich chemicals, USA), Nitric acid (HNO_3, 70% , Sigma Aldrich chemicals, USA) and sodium hydroxide (NaOH, 98%, Sigma Aldrich chemicals, USA) were used as received. House distilled water was further purified through a Milli-Q (Millipore) filtration system. Acetone and ethanol were purchased from VWR. Si /SiO_2 were purchased from Sigma Aldrich. Anodic aluminum oxide membrane (AAO) of pore diameter ~80 nm, pore length ~100 μm was purchased from In Redox materials innovation and Polycarbonate membrane of pore diameter ~47 nm and pore length ~6 μm was purchased from Millipore Sigma.

Synthesis of Bi_2Te_3, Sb_2Te_3 and p-n junction NWs

In this work, we used two different types of membrane for template synthesis as required: Anodic aluminum oxide membrane (AAO) and Polycarbonate membrane. An AAO membrane was used for NWs formation in the following manner: first, through a mask, 100 nm of Au is sputtered on one side of the membrane using a sputtered coater (Quorum QT50TS) at 40 mA, to serve as a cathode (working electrode). The working electrode, is then connected with Ag paste, to Cu leads on a Plexiglas sample holder made in house. The

contact electrode is then connected, with Au foil strips and Ag paste to another Cu leads on the same substrate. This assembly is wrapped in Kapton tape with the working electrode is exposed by an opening previously cut in the tape. The edges of the exposed contact electrode are sealed with nail polish. The exposed area of the membrane is a 0.2 cm^2 circle. The same protocol was used for polycarbonate membrane [Wade and Wegrowe, 2005].

Electrodeposition of Bi_2Te_3, Sb_2Te_3 and p-n junction NWs

These NWs were fabricated by direct-current electrodeposition into AAO /polycarbonate membrane sample as prepared above. The plating solution was prepared by dissolving Te, Bi and Sb into 1 M HNO_3 was mixed for 24 hours at room temperature then the solution was diluted to desired volume with distilled water. The electrodeposition using AAO (50μm thick) was carried out at a constant potential of -62 mV for 1500 s for Bi_2Te_3 NWs and -300 mV for 2000 s for Sb_2Te_3 relative to an Ag/AgCl reference electrode at room temperature while for polycarbonate (6μm thick) the constant potential was for 500s and 650s for Bi_2Te_3 and Sb_2Te_3 respectively. A pure Au wire was used as a counter electrode and AAO/polycarbonate membrane was used as a working electrode. Crystalline NWs were obtained by dissolving the AAO and polycarbonate membrane with 2 M aqueous. NaOH solution and dichloromethane respectively. The as obtained product is centrifuged followed by washing with deionized water three-four times. The whole procedure is shown in [Figure S8]. For p-n junction nanowire we deposited n- type Bi_2Te_3 with constant potential of -62 mV, time 500s in half of the wire and another half we deposited p-type Sb_2Te_3 with constant potential of -300 mV, time 1000s. For polycarbonate membrane, the time was 50 s for Bi_2Te_3 and 100 s for Sb_2Te_3.

Characterizations

The structural properties of the NWs were analyzed by X-ray diffraction (XRD), (XRD, D8 Advance, Bruker AXS) dedicated to thin film analysis, in a parallel beam geometry (ω-2θ) equipped with Cu radiation (Kα1 = 1.54178 Å). The data collection was performed from 21 to 50, 2θ, with a step of 0.03° and 15 seconds per step. Phase identification was performed with the highscore software (PANalytical) and powder diffraction files (ICDD PDF2 2004 and COD databases) [Grazulis et al., 2009]. Morphological properties of the wires were analyzed with Scanning electron microscopy (SEM) Hitachi S-4800. The SEM imaging was performed at 10 kV and the sample were made by a solution of NWs was dispersed in 0.5 mL of absolute ethanol. A droplet was then drop cast onto a silicon substrate and naturally dried in air for 20 min.

Selected Area Electron Diffraction (SAED) have been acquired on a JEOL 2010F operating at 200 kV. Scanning- TEM (STEM) experiments have been performed on a probe-corrected field emission gun FEI Titan Themis microscope operating at 200 kV (probe size 1Å). This microscope is equipped with the''Super-X'' detector permitting quantitative elemental mapping of Sb, Bi and Te (Cliff-Lorimer methods) by EDX.'' The sample preparation for TEM was the same as for SEM except that the drop cast onto a Cu coated TEM grid (agar scientific.).